CrossMark

Turbulent Model of Crab Nebula Radiation

Yonggang Luo[1], Maxim Lyutikov[1] , Tea Temim[2] , and Luca Comisso[3]
[1] Department of Physics and Astronomy, Purdue University, 525 Northwestern Avenue, West Lafayette, IN 47907, USA
[2] Space Telescope Science Institute, 3700 San Martin Drive, Baltimore, MD 21218, USA
[3] Department of Astronomy, Columbia University, 550 W 120th Street, New York, NY 10027, USA
Received 2020 March 15; revised 2020 May 13; accepted 2020 May 14; published 2020 June 23

Abstract

We construct a turbulent model of the Crab Nebula's nonthermal emission. The present model resolves a number of long-standing problems of the Kennel–Coroniti model: (i) the sigma problem, (ii) the hard spectrum of radio electrons, (iii) the high peak energy of gamma-ray flares, (iv) and the spatial evolution of the infrared (IR) emission. The Nebula contains two populations of injected particles: Component-I, accelerated at the wind termination shock via the Fermi-I mechanism; and Component-II, accelerated in reconnecting turbulence in highly magnetized ($\sigma \gg 1$) plasma in the central part of the Crab Nebula. The reconnecting turbulence in Component-II extends from radio to gamma-rays: it accelerates radio electrons with a hard spectrum, destroys the large-scale magnetic flux (and thus resolves the sigma problem), and occasionally produces gamma-ray flares (from the largest-scale reconnection events). The model reproduces the broadband spectrum of the Crab Nebula, from low-frequency synchrotron emission in radio to inverse-Compton emission at TeV energies, as well as the spatially resolved evolution of the spectral indices in the IR and optical bands.

Unified Astronomy Thesaurus concepts: Rotation powered pulsars (1408); Stellar wind bubbles (1635); Interstellar synchrotron emission (856)

1. Introduction

1.1. The Kennel–Coroniti Model: Its Success, Problems, and Resolution

The Crab Nebula is the paragon of high-energy astrophysical sources—understanding particle acceleration in the Crab has implications for other sources, like active galactic nuclei and gamma-ray bursts. Conventionally, particles in the pulsar wind nebulae (PWNs) are assumed to be accelerated at the pulsar wind termination shock (Rees & Gunn 1974; Kennel & Coroniti 1984a, 1984b; Atoyan & Aharonian 1996). The inferred particle spectral index $p = 2.2$, derived from the nonthermal X-ray synchrotron spectrum, matches the expectations for the Fermi-I mechanism (e.g., Blandford & Eichler 1987). In addition, numerical magnetohydrodynamics (MHD) simulations (del Zanna et al. 2004; Komissarov & Lyubarsky 2004; Porth et al. 2014, 2017), with the assumed particle acceleration at the termination shock, reproduce well the overall X-ray morphology of the PWNs.

However, there are clear drawbacks to the Kennel & Coroniti (1984a, 1984b) model. The origin of the radio-emitting particles is not addressed. The radio spectrum of the Crab PWN has a spectral index of $\alpha = 0.3$ (Bietenholz et al. 1997; Reynolds et al. 2017), which implies a particle spectral index of $p = 1.6$ for an isotropic distribution of nonthermal electrons. Such a hard radio emission is not consistent with the Fermi-I acceleration mechanism (assumed to be operational at the termination shock), which typically gives $p > 2$ (e.g., Blandford & Eichler 1987). In addition, the lowest observed radio emission from the Crab Nebula, down to 100 MHz, requires Lorentz factors of only 10^2, well below the typically expected wind Lorentz factor of $\gamma_w \sim 10^4$–10^6 (e.g., Arons 2007, 2012).

The second major problem in modeling the Crab Nebula's emission, identified by Rees & Gunn (1974) and Kennel & Coroniti (1984a), is the is so-called sigma problem: models of

pulsar magnetospheres (Fawley et al. 1977; Harding & Muslimov 1998; Hibschman & Arons 2001) predict $\sigma \gg 1$, where sigma is the conventional magnetization parameter (Kennel & Coroniti 1984a). Supersonic flows with $\sigma \gg 1$ (carrying a large-scale magnetic field) cannot be accommodated by the nonrelativistically expanding nebula. The resolution to the sigma problem is the destruction of the large-scale magnetic flux, either in the wind (Coroniti 1990; but see Lyubarsky & Kirk 2001) or in the turbulent post-shock flow (Lyutikov & Blandford 2003; Lyutikov 2006; Porth et al. 2013; Zrake & Arons 2017; Tanaka et al. 2018). We accept the latter interpretation; see Section 2.

The third problem with the Kennel & Coroniti (1984a) model is related to Crab's gamma-ray flares (Abdo et al. 2011; Tavani et al. 2011; Buehler et al. 2012). As discussed by Lyutikov (2010; before the discovery of the flares) and Clausen-Brown & Lyutikov (2012; see also de Jager et al. 1996), the peak energy of flares—as high as 400 MeV— violates the synchrotron limit and is inconsistent with the slow Fermi-I-type acceleration at the shock front. Reconnection in magnetically dominated plasma may accelerate particles at a much faster rate, resolving the problem of the high peak energy of flares (Zenitani & Hoshino 2001; Lyutikov & Uzdensky 2003; Lyubarsky 2005; Lyubarsky & Liverts 2008; Lyutikov 2010; Clausen-Brown & Lyutikov 2012; Hoshino & Lyubarsky 2012; Komissarov 2012; Cerutti et al. 2014b; Lyutikov et al. 2017a, 2017b, 2018).

The fourth problem with the Kennel–Coroniti model is that it is in significant conflict with the observed radial–spectral dependence of the PWNs (Reynolds 2009; Reynolds et al. 2017). Models predict a drop in size of the PWN by at least a factor of 2 between radio and X-ray wavelengths, but observed PWNs do not show this behavior.

We suggest a common resolution to all the problems mentioned above (the spectrum of radio electrons, the sigma problem, the high peak energy of gamma-ray flares, and the

resolved spectral evolution). We foresee that there are two nonthermally emitting components in the Nebula: one (Component-I) is accelerated at the termination shock, and another (Component-II) is accelerated in relativistic reconnection events in the bulk of the Nebula, as argued by Lyutikov et al. (2019); see also Comisso & Sironi (2018). Component-I abides by the rules of the Kennel & Coroniti (1984a, 1984b) model, with low magnetization in the equatorial part of the wind. Component-II results from the highly magnetized plasma turbulence, which increases the rate of reconnection (Matthaeus & Lamkin 1986) in the bulk of the nebula and destroys the magnetic flux in reconnection events. The largest reconnection events result in gamma-ray flares (Clausen-Brown & Lyutikov 2012).

In Section 2, we discuss the sigma problem from the point of view of the conservation of large-scale magnetic flux. In Section 3, we construct a turbulent model of PWNs. In Section 4, we consider the evolution of particles in a changing magnetic field of the Nebula. In Section 5, we discuss the particle acceleration mechanisms in magnetically dominated reconnecting turbulence. In Section 6, we construct the turbulent model of the Crab Nebula radiation. In Section 7, we construct the corresponding spectral maps in the infrared (IR) and optical and compare them with observational data.

2. The Sigma Problem: The Problem of the Magnetic Flux

To clarify the sigma problem and to highlight its resolution (Lyutikov & Blandford 2003; Lyutikov 2006), let us consider a central source (a neutron star) that injects into the Crab Nebula a highly magnetized, $\sigma \sim 1$, relativistic (supersonic—hence causally disconnected from the source) flow that carries a large-scale toroidal magnetic field. If at the injection radius r_{in} (~light cylinder) the magnetic field is B_{in}, then the magnetic energy is injected at the rate of

$$\frac{dE_B}{dt} \sim B_{in}^2 r_{in}^2 c \qquad (1)$$

(for $\sigma \sim 1$, dE_B/dt is of the order of the spin-down luminosity). The total injected energy is then

$$E_B = B_{in}^2 r_{in}^2 ct. \qquad (2)$$

At the same time, the central source injects magnetic flux, integrated over half the cross section of the Nebula, at the rate of

$$\frac{d\Phi}{dt} \sim B_{in} r_{in} c. \qquad (3)$$

(The total injected flux, integrated over the whole cross section of the Nebula, is zero, with two opposite contributions of the value (4) through two east–west cross sections.) The total flux, integrated over half a cross section, stored in the nebula is

$$\Phi_{tot} \sim B_{in} r_{in} ct. \qquad (4)$$

If the cavity expands with velocity V_{PWN}, the magnetic field and the energy in the bulk are

$$B \sim \frac{\Phi_{tot}}{(V_{PWN}t)^2} = \frac{cB_{in}r_{in}}{tV_{PWN}^2}$$

$$E_{stored} \sim B^2(V_{PWN}t)^3 = \frac{B_{in}^2 r_{in}^2 c^2 t}{V_{PWN}}. \qquad (5)$$

Comparing Equations (2) and (5), the injected and the stored energy, it is then required that $V_{PWN} \sim c$—only relativistically

expanding nebula can accommodate the injected flux. Because PWNs expand nonrelativistically our assumption that a central source injects a highly magnetized relativistic flow leads to an inconsistency—this is the sigma paradox. Only weakly magnetized flows, with magnetic energy flux much smaller than the total wind luminosity by $\sigma \sim V_{PWN}/c$, can be matched to the nonrelativistically expanding boundary (Kennel & Coroniti 1984a).

This exercise also suggests a resolution of the sigma paradox: what is needed is the destruction of the large-scale magnetic flux (but not necessarily of the magnetic field!). Consider a large-scale magnetic loop, which has zero total toroidal flux composed of two opposite contributions in the two east–west cross sections. If the loop is broken into small loops, the total flux remains zero, but also now the flux is zero through any east–west cross sections. Relation (3) is then no longer valid—there is then no sigma paradox.

Thus, if the magnetic field is converted into small-scale structures, it would behave as a fluid with some specific equation of state. For example, if a "fluid" is composed of magnetic bubbles, then the conservation of flux within a bubble would produce a magnetic pressure

$$B^2 \propto V_b^{-4/3} \qquad (6)$$

where V_b is the volume of a bubble. This scaling is reminiscent of a relativistic fluid with an adiabatic index of $4/3$. Porth et al. (2013) indeed demonstrated numerically that the development of current-driven instabilities in the post-termination shock region leads to the resolution of the sigma problem.

Given the above arguments, we conclude that instead of the smooth flow imagined by Kennel & Coroniti (1984a), the PWNs must be highly turbulent. Below we develop a magnetohydrodynamic and radiation model of a PWN, assuming it is dominated by turbulence. Previously, a number of models took into account turbulence and the ensuing diffusion on top of the Kennel–Coroniti flow (e.g., Gratton 1972; Reynolds & Jones 1991; Tang & Chevalier 2012; Porth et al. 2016). Here we take the extreme position that magnetohydrodynamic turbulence dominates the flow. This is surely an extreme assumption: in reality, the flow is partially magnetic flux conserving (as demonstrated by large-scale polarization structures that imply toroidal magnetic field; Dean et al. 2008) and partially turbulent. Yet, as we argue, this extreme 1D model does reproduce various observational phenomena and resolve the problems of the Kennel–Coroniti model.

3. Confinement of the Turbulent Crab Nebula PWN by Its Supernova Remnant

As we argued above, destruction of the magnetic flux is needed to resolve the sigma problem. This is achieved via reconnecting turbulence in the post-shock flow. In this section, we construct a turbulent model of PWNs, whereby the post-shock flow quickly becomes highly turbulent, thus losing the extra requirement of magnetic flux conservation. We consider an extreme case of complete destruction of the magnetic flux. Naturally, this is an approximation—the real PWN does keep some toroidal magnetic flux, as illustrated by polarized emission from high energy (Dean et al. 2008; Chauvin et al. 2016, 2017, 2018), to microwaves (Planck Collaboration et al. 2018; Ritacco et al. 2018), to the radio (Bietenholz & Kronberg 1991).

3.1. Overall Expansion

Consider a central source producing a relativistic supersonic wind with luminosity L_w, confined within a homologously expanding stellar envelope. Let us first estimate the overall dynamics of the bubble in the early stages of expansion, when the reverse shock in the ejecta has not yet reached the expanding PWN.

The stellar envelope ejected during the supernova explosion expands homologously, so that its density evolves according to

$$\rho = \frac{3}{4\pi}\frac{M_{ej}}{(V_{ej}t)^3}$$
$$E_{ej} = \frac{3}{10}M_{ej}V_{ej}^2,$$
$$v_r = \frac{r}{t}, \; r \leqslant V_{ej}t, \qquad (7)$$

where M_{ej} is ejecta mass and V_{ej} is the maximal velocity; a more general scaling of ρ can also be used, $\rho \propto t^{-3}f(r/t)$, $v_r \propto (r/t) f(r/t)$.

Conventionally (e.g., Chevalier 2005), the dynamics of the PWN is treated in what could be called a Sedov approximation, whereby the internal pressure of the nebula drives supersonic expansion into the supernova ejecta. (Roughly speaking, the Sedov approximation is applicable if the size of the termination shock in the pulsar wind is much smaller than the size of the PWN.) In this case, the mass, momentum, and energy conservation equations are

$$\partial_t M = 4\pi R^2 \rho \left(V - \frac{R}{t}\right)$$
$$M\partial_t V = 4\pi R^2 \left(p - \rho\left(V - \frac{R}{t}\right)^2\right)$$
$$\partial_t(4\pi p R^3) = L_w - 4\pi R^2 V p$$
$$V = \partial_t R \qquad (8)$$

(p and ρ are the pressure and density internal to the expanding PWN, L_w is the wind luminosity, and V is the overall velocity of expansion.).

The wind luminosity is given by the pulsar spin-down power:

$$L_w = \frac{I_{NS}\tau\Omega_0^4}{2(1 + t\tau\Omega_0^2)^2}$$
$$\tau = 2\frac{B_{NS}^2 R_{NS}^6}{I_{NS}c^3}$$
$$\Omega = \frac{\Omega_0}{\sqrt{1 + t\tau\Omega_0^2}} = \frac{\Omega_0}{\sqrt{1 + t/t_0}}$$
$$t_0 = \frac{c^3 I_{NS}}{2B_{NS}^2 R_{NS}^6 \Omega_0^2}, \qquad (9)$$

where I_{NS} is the moment of inertia of the neutron star, Ω_0 is the initial spin, Ω is the current spin, $B_{NS} = 4 \times 10^{12}$ G is the surface magnetic field, and $R_{NS} = 10^6$ cm is the radius of the neutron star.

As a simplifying assumption in our 1D model, we ignore the evolution of the spin-down power and assume $L_w \sim$ constant. This assumption excludes possible extremely high initial spins, as suggested by Atoyan (1999; so that the population of radio

electrons now is dominated by particles injected very early in the evolution). Higher luminosity at earlier times will mildly affect (slightly underestimate) the population of radio-emitting electrons.

Assuming constant wind power the corresponding scaling are

$$R_{PWN} = 0.38\left(\frac{L_w V_0^5}{E_{ej}}\right)^{1/5} t^{6/5} = R_{PWN,now}\left(\frac{t}{t_{now}}\right)^{6/5}$$
$$M = 22.4\left(\frac{E_{ej}^2 L_w^3}{V_0^{10}}\right)^{1/5} t^{3/5}$$
$$p = 0.064\left(\frac{E_{ej}^3 L_w^2}{V_0^3}\right)^{1/5} t^{-13/5}, \qquad (10)$$

where R_{PWN} is the radius of the PWN, M is the swept-up mass, and p is the pressure.

3.2. Internal Velocity Structure of Turbulent PWN Flow

Let us adopt a limiting case, where instead of the smooth flow envisioned by Kennel & Coroniti (1984a) the requirement of magnetic flux destruction leads to a completely turbulent flow in the nebula. The turbulent magnetic field behaves as a fluid, with some specific equation of state, Equation (6). The post-shock plasma is relativistically hot, with the sound speed $c_s \sim c/\sqrt{3}$. The post-shock evolution of the fluid (mixture of relativistic plasmas and turbulent magnetic field) will then quickly reach subrelativistic velocities and, hence, an incompressible limit.

Consider an incompressible flow within a sphere expanding according to Equation (10). Looking for the flow velocity of the incompressible fluid in the form $v(r, t) = V_{ej}(t) f(x)$ with $x = r/R_{PWN}(t)$, we find

$$v = \frac{6}{5}\frac{R_{PWN,now}^3 t^{13/5}}{r^2 t_{now}^{18/5}} \qquad (11)$$

(this satisfies the condition div $\mathbf{v} = 0$ and matches the boundary expansion). Equation (11) gives the velocity of the fluid element located at time t at a distance r; it is parameterized to the size $R_{PWN,now}$ and age t_{now} of the Crab Nebula now.

The flow should also match the post-termination-shock conditions (e.g., $v_{term.shock} = c/3$ in the purely fluid regime). Clearly, this cannot be done in a mathematically meaningful sense—the system becomes overdetermined. Still, the estimated location of the termination shock,

$$\frac{r_{term.shock}}{R_{PWN,now}} \approx \sqrt{\frac{R_{PWN,now}}{ct_{now}}} \approx 0.1, \qquad (12)$$

is a reasonable estimate of the relative size of the termination shock with respect to the overall Nebula. Recall that one of the effects of the sigma problem within the model of Kennel & Coroniti (1984a) was that the size of the termination shock becomes too small for $\sigma \to 1$. The turbulent model avoids that problem. We consider this as a major advantage of the model.

Consider next a shell ejected at time t_{ej} from the termination shock of radius R_{ej}. Integrating equation of motion (11) with

$v = dr/dt$, the location of the shell at time t is

$$\frac{r_{\text{shell}}}{R_{\text{PWN,now}}} = \left(\left(\frac{R_{\text{ej}}}{R_{\text{PWN,now}}}\right)^3 + \left(\frac{t}{t_{\text{now}}}\right)^{18/5} - \left(\frac{t_{\text{ej}}}{t_{\text{now}}}\right)^{18/5}\right)^{1/3}$$

$$\rightarrow \left(\left(\frac{R_{\text{ej}}}{R_{\text{PWN,now}}}\right)^3 + 1 - \left(\frac{t_{\text{ej}}}{t_{\text{now}}}\right)^{18/5}\right)^{1/3}. \tag{13}$$

(A a check, for $t_{\text{ej}} = 0$ and $R_{\text{ej}} = 0$, Equation (13) reproduces Equation (10)). The last equality in Equation (13) refers to the present time, $t = t_{\text{now}}$.)

A shell located at $r_{\text{shell,now}}$ at present time has been ejected at time

$$\frac{t_{\text{ej}}}{t_{\text{now}}} = \left(1 + \left(\frac{R_{\text{ej}}}{R_{\text{PWN,now}}}\right)^3 - \left(\frac{r_{\text{shell,now}}}{R_{\text{PWN,now}}}\right)^3\right)^{5/18}. \tag{14}$$

3.3. Magnetic Field within the Shell

At each moment. the amount of energy injected by the pulsar should balance the nebula pressure, given by the sum of magnetic and kinetic pressures p_k. (Plasma within the Nebula is relativistically hot, hence we can ignore the energy of the bulk motion which is smaller by a factor of $(v/c)^2$ than the combined enthalpy.)

Using Equation (10) with the total pressure given by the sum of kinetic and magnetic pressures,

$$p_{\text{tot}} = \frac{B^2}{8\pi} + p_k = \frac{B^2}{8\pi}(1 + \beta), \tag{15}$$

where β is the plasma beta parameter, the magnetic field within a nebula at time t is then

$$B(t) = B_{\text{now}}\left(\frac{t}{t_{\text{now}}}\right)^{-13/10}$$

$$B_{\text{now}} = 16.4 \frac{E_{\text{ej}}^{3/10} L_w^{1/5}}{V_0^{3/2}\sqrt{1+\beta}} t_{\text{now}}^{-13/10} = \frac{\sqrt{6L_w t_{\text{now}}}}{R_{\text{PWN,now}}^{3/2}}$$

$$\approx 6 \times 10^{-4} \text{ G}, \tag{16}$$

where the last estimate assumes ejecta energy $E_{\text{ej}} = 10^{51}$ erg, maximum velocity $V_0 = 7500$ km s^{-1}, and $\beta = 10^2$.

Given the nature of the order-of-magnitude estimates, the above values are very close to the estimates of the magnetic field in the Nebula (e.g., Reynolds et al. 2017). We consider this as another major advantage of the model.

4. Particle Distribution within the Nebula

Above, we constructed a fluid-like turbulent model of PWN, composed of shells of material injected at different times. The magnetic field in each shell evolves with time according to Equation (16). In this section, we calculate the radiation signatures of such turbulent PWNs. In Section 4.1, we consider the evolution of the particle distribution within each injected shell, taking into account radiative losses (there are no adiabatic losses in the incompressible approximation).

In Section 4.1, we find the Green's function for particles injected at some moment and experiencing radiative decay in an evolving magnetic field. The Green's function, multiplied by

the injection rate, gives the particle distribution function within each shell. Next, in Section 4.2, we integrate the Green's function over the injection time to find the total particle distribution within the Nebula.

4.1. Evolution of the Particle Distribution in a Changing Magnetic Field

We assume that particles are injected into the inner regions of the PWN with some given distribution and seek to find the particle distribution within each injected shell, taking into account radiative losses and a changing magnetic field within each shell. We need to solve the Boltzmann (Liouville) equation for the Green's function, G,

$$\frac{\partial G}{\partial t} = \frac{\partial(\dot{\gamma}G)}{\partial\gamma} + f_{\text{inj}}\delta(t - t_{\text{inj}}), \tag{17}$$

for an injected spectrum with a power-law particle distribution

$$f_{\text{inj}} \propto \gamma_{\text{inj}}^{-p}, \ \gamma > \gamma_{\text{inj,min}}, \tag{18}$$

where t_{inj} is the moment of injection and $\gamma_{\text{inj,min}}$ is the minimum injection Lorentz factor.

Consider first the evolution of the Lorentz factor of the particles experiencing radiative losses in an evolving magnetic field,

$$\dot{\gamma} = -\frac{4}{9}\frac{e^2}{m_e c^3}\gamma^2\omega_B^2$$

$$\omega_B = \frac{eB}{m_e c}$$

$$B = B_0\left(\frac{t}{t_0}\right)^{-\delta} \tag{19}$$

with $\delta > 1/2$. (In our case, $\delta = 13/10$; see Equation (16).) For definiteness, we can set $t_0 = t_{\text{now}}$, so that $t < t_0$.

Introducing

$$\tau_c = \frac{9}{4}\frac{m_e^3 c^5}{e^4 B_{\text{now}}^2}$$

$$\gamma_M = \frac{\tau_c}{t_{\text{now}}}, \tag{20}$$

Equation (19) can be written as

$$\dot{\gamma} = -\left(\frac{t_{\text{now}}}{t}\right)^{2\delta}\frac{\gamma^2}{t_{\text{now}}\gamma_M}. \tag{21}$$

If at time t_{inj} a particle was injected with Lorentz factor γ_{inj}, then the Lorentz factor evolves according to

$$\frac{\gamma}{\gamma_{\text{inj}}} = \left(1 + \frac{1}{2\delta - 1}\left(\left(\frac{t_{\text{now}}}{t_{\text{inj}}}\right)^{2\delta-1} - \left(\frac{t_{\text{now}}}{t}\right)^{2\delta-1}\right)\frac{\gamma_{\text{inj}}}{\gamma_M}\right)^{-1}$$

$$\frac{\gamma_{\text{inj}}}{\gamma} = \left(1 - \frac{1}{2\delta - 1}\left(\left(\frac{t_{\text{now}}}{t_{\text{inj}}}\right)^{2\delta-1} - \left(\frac{t_{\text{now}}}{t}\right)^{2\delta-1}\right)\frac{\gamma}{\gamma_M}\right)^{-1}. \tag{22}$$

For a given time t, the Lorentz factor must be smaller than

$$\gamma_{\text{max}}(t) = (2\delta - 1)\left(\left(\frac{t_{\text{now}}}{t_{\text{inj}}}\right)^{2\delta-1} - \left(\frac{t_{\text{now}}}{t}\right)^{2\delta-1}\right)^{-1}\gamma_M \tag{23}$$
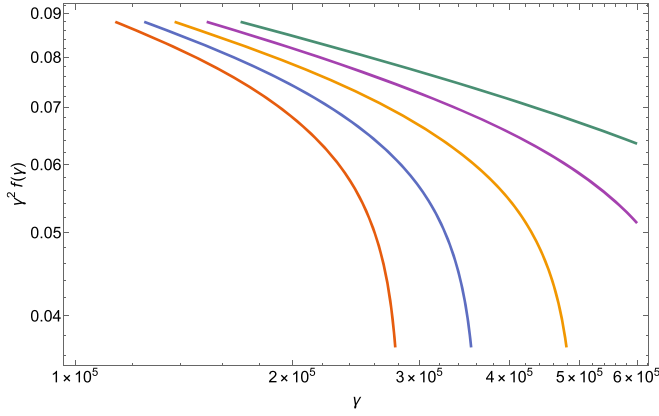
Figure 1. Evolution of the distribution function within one shell. Each line has the injection time t_{inj} as $t_{now}/t_{inj} =$ 1.1, 1.2, 1.3, 1.4, and 1.5 (from green to red) with the same minimum injection Lorentz factor $\gamma_{inj,min}$ and normalization factor. As the particle distribution function evolves with time, particles are cooled due to synchrotron emission and shifted to lower energy. Here, the power-law index $p = 2.2$ and the minimum injection Lorentz factor $\gamma_{inj,min} = 1.9 \times 10^5$.

Figure 2. Total particle distribution function within the Nebula for different present-time magnetic fields: 2.0×10^{-4} G (red), 2.5×10^{-4} G (blue), 3.0×10^{-4} G (orange), 3.5×10^{-4} G (purple), and 4.0×10^{-4} G (green) at t_{now}. We keep injecting a power-law particle distribution from injection time $t_{inj} = 0.1 \times t_{now}$ with $p = 2.2$ and the same minimum Lorentz factor $\gamma_{inj,min} = 1.9 \times 10^5$, and let all particles evolve with time. All curves are normalized to unity at the injection break.

and larger than

$$\gamma_{min}(t) = \left(1 + \frac{1}{2\delta - 1}\left(\left(\frac{t_{now}}{t_{inj}}\right)^{2\delta - 1}\right.\right.$$
$$\left.\left. - \left(\frac{t_{now}}{t}\right)^{2\delta - 1}\right)\frac{\gamma_{inj,min}}{\gamma_M}\right)^{-1}\gamma_{inj,min}. \quad (24)$$

Thus, at any time t, the distribution function for particles injected at t_{inj} is given by

$$G(t, t_{inj}) \propto \gamma^{-p}\left(1 - \frac{1}{2\delta - 1}\left(\left(\frac{t_{now}}{t_{inj}}\right)^{2\delta - 1} - \left(\frac{t_{now}}{t}\right)^{2\delta - 1}\right)\frac{\gamma}{\gamma_M}\right)^{p-2}$$
$$\times \Theta(\gamma - \gamma_{min}(t))\Theta(\gamma_{max}(t) - \gamma); \quad (25)$$

see Figure 1. Equation (25) gives the Green's function for the evolution of the particle distribution function. There is a special injection time $t_{inj,full}$ so that now, at $t = t_{now}$, for $t_{inj} < t_{inj,full}$, the highest possible Lorentz factor becomes smaller than the minimum injection Lorentz factor $\gamma_{inj,min}$: in this regime, all the particles enter the fast cooling regime:

$$\frac{t_{inj,full}}{t_{now}}$$
$$= \left(1 + (2\delta - 1)\frac{\gamma_M}{\gamma_{inj,min}}\right)^{-1/(2\delta-1)} \rightarrow \left(1 + \frac{\gamma_M}{\gamma_{inj,min}}\right)^{-1}. \quad (26)$$

If $t_{inj} < t_{inj,full}$, then all the particles within a shell cool below $\gamma_{inj,min}$. Because $\gamma_M \leqslant \gamma_{inj,min}$, most of the particles that have been accelerated above $\gamma_{inj,min}$ over the lifetime of the Nebula had time to cool down below $\gamma_{inj,min}$.

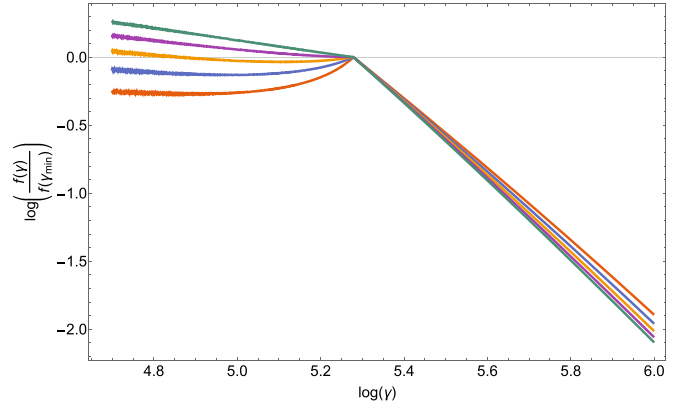The ratio $\gamma_{max}/\gamma_{min}$ is

$$\frac{\gamma_{max}}{\gamma_{min}} = 1 + (2\delta - 1)\left(\left(\frac{t_{now}}{t_{inj}}\right)^{2\delta - 1} - \left(\frac{t_{now}}{t}\right)^{2\delta - 1}\right)^{-1}$$
$$\times \frac{\gamma_M}{\gamma_{inj,min}}. \quad (27)$$

For earlier $t_{inj} \rightarrow 0$, the ratio $\gamma_{max}/\gamma_{min} \rightarrow 1$. Thus, with time, all the particles injected at some t_{inj} occupy a narrower and narrower range of $d\gamma$—there is an effective pile-up in the distribution.

4.2. The Overall Particle Distribution in the Crab Nebula

Equation (25) describes the evolution of the distribution function for the particles injected at time t_{inj}. To find the total distribution function in the Nebula, the Green's function, Equation (25), should be integrated over injection times $t_{inj} \leqslant t_{now}$. Results of the numerical integration are plotted in Figure 2 (constant injection parameters are assumed).

In Figure 2, there is one injection break at $\gamma_{inj,min}$ for all curves as they all have the same minimum injection Lorentz factor. For large magnetic fields (e.g., purple and green curves), particles cool quickly, so that the distribution increases below the injection break toward smaller Lorentz factors and has a relatively higher number of particles at lower energy. For small magnetic fields (e.g., red, blue, and orange curves), the distribution is nearly constant and has a relatively lower number of particles at lower energies, which are the particles cooled quickly early on when the magnetic field was strong.

5. Acceleration in Relativistic Reconnecting Turbulence

In addition to providing a satisfactory solution to the sigma problem, magnetized turbulence in the bulk of the Crab Nebula is expected to accelerate particles far out of thermal equilibrium.[4] Particle acceleration can occur due to a

---

[4] To be clear, our model is different from the "turbulent reconnection" of Lazarian & Vishniac (1999); in that case "turbulent reconnection" is understood as turbulence inside a reconnecting current sheet. In contrast, what we envision can be described as turbulence with reconnection occurring in various current sheets inside the turbulence itself.

combination of turbulence fluctuations and magnetic reconnection events that are self-consistently produced by the turbulent motions in the plasma. Indeed, in magnetized turbulence, contrary to hydrodynamic turbulence, the presence of the magnetic field gives rise to turbulence eddies that become progressively more anisotropic toward small scales within the inertial range, producing current-sheet-like structures that are prone to magnetic reconnection (Carbone et al. 1990; Loureiro & Boldyrev 2017; Mallet et al. 2017; Comisso et al. 2018) due to the plasmoid instability that kicks in while the current sheets are forming (Comisso et al. 2016, 2017; Uzdensky & Loureiro 2016).

Recent first-principle kinetic simulations (Comisso & Sironi 2018, 2019) have shown that in a strongly magnetized plasma ($\sigma \gg 1$), such as the case for the central part of the Crab Nebula, the interplay between turbulence fluctuations and magnetic reconnection leads to the generation of a large fraction of nonthermal particles. The resulting particle energy distribution had been shown to display a power-law energy tail $dn/d\gamma \propto \gamma^{-p}$ that extends well beyond the Lorentz factor

$$\gamma \sim (1 + \sigma)\gamma_0, \tag{28}$$

which takes into account the fact that most of the magnetic energy is converted to particle energy by the time the particle energy spectrum has saturated (Comisso & Sironi 2018, 2019). The slope p of the particle energy spectrum was found to depend on the plasma magnetization σ and the amplitude of the turbulence fluctuations $\delta B_{\rm rms}$ with respect to the mean magnetic field B_0. In particular, the power-law slope p is harder for larger magnetizations and stronger turbulence fluctuations (Zhdankin et al. 2017; Comisso & Sironi 2018, 2019). For $\sigma \gg 1$ and large turbulent fluctuations ($\delta B_{\rm rms}^2/B_0^2 \sim 6$ in some regions of the Crab Nebula, as discussed in Lyutikov et al. 2019), the power-law slope was found to be $p < 2$ (Comisso & Sironi 2018, 2019), but generally not as hard as the slope generated by reconnection alone with the same parameters, which can approach $p \to 1$ for $\sigma \gg 1$ (Zenitani & Hoshino 2001; Guo et al. 2014; Sironi & Spitkovsky 2014; Werner et al. 2016; Lyutikov et al. 2017a, 2017b). Therefore, it is conceivable to assume a space-averaged spectrum with a slope $p \sim 1.6$, as can be inferred from the radio spectrum of the Crab Nebula.

More specifically, Comisso & Sironi (2018, 2019) have shown that plasmoid-mediated reconnection controls the initial acceleration of particles from the thermal bath at γ_0 up to the Lorentz factor $\gamma_0(1 + \sigma)$. In our model, γ_0 corresponds to the wind Lorentz factor in the absence of dissipation. Then, some particles are further accelerated to much higher energies by stochastic interactions with turbulent fluctuations, with the most energetic particles reaching

$$\gamma_{\rm max} \sim \frac{eB_{\rm rms}\ell}{m_e c^2}, \tag{29}$$

where ℓ indicates the size of the largest turbulent eddies and $B_{\rm rms}$ is the space-averaged rms value of the magnetic field. This two-stage acceleration process is characterized by a combination of systematic (Fermi-I) and stochastic (Fermi-II) particle acceleration mechanisms.

At small scales, the nonideal reconnection electric fields, whose magnitude is $|E_\parallel| \simeq \beta_R \delta B_{\rm rms}$, accelerate particles according to

$$\frac{d\langle\gamma\rangle}{dt} = \frac{e}{m_e c}\beta_R \delta B_{\rm rms}, \tag{30}$$

where β_R is the average reconnection rate, which is an $O(0.1)$ quantity for relativistic collisionless plasmas (Zenitani et al. 2009; Bessho & Bhattacharjee 2012; Cerutti et al. 2012; Guo et al. 2014; Kagan et al. 2015; Liu et al. 2015; Comisso & Bhattacharjee 2016; Sironi et al. 2016; Lyutikov et al. 2017a; Werner & Uzdensky 2017). The fast reconnection rate $\beta_R \sim 0.1$ guarantees that magnetic reconnection can process large volumes of plasma in a few outer-scale eddy turnover times, in addition to enabling particle acceleration on a fast timescale $t_{\rm acc} \sim \beta_R^{-1}\rho_{\rm L}/c$, where $\rho_{\rm L}$ is the particle Larmor radius.

After the initial acceleration due to plasmoid-mediated reconnection, particles are further accelerated by stochastic scattering off turbulent fluctuations in the inertial range of the turbulent energy cascade. The mean particle energy gain due to stochastic acceleration is related to the diffusion coefficient in energy space as

$$\frac{d\langle\gamma\rangle}{dt} = \frac{1}{\gamma^2}\frac{\partial}{\partial\gamma}(\gamma^2 D_{\gamma\gamma}), \tag{31}$$

with an energy diffusion coefficient $D_{\gamma\gamma}$ that depends on the instantaneous plasma magnetization and the particle Lorentz factor as (Comisso & Sironi 2019)

$$D_{\gamma\gamma} \sim 0.1\sigma\left(\frac{c}{l}\right)\gamma^2, \tag{32}$$

akin to the original Fermi-II mechanism (e.g., Blandford & Eichler 1987; Lemoine 2019). Note that the timescale $t_{\rm acc}$ of the stochastic acceleration process is comparable to that of fast plasmoid-mediated reconnection in the strong turbulence scenario considered here. Indeed, the stochastic acceleration timescale is $t_{\rm acc} \sim \gamma^2/D_{\gamma\gamma} \sim 10\,\ell/\sigma c$, with σ being the instantaneous magnetization. The instantaneous magnetization decreases rapidly in time as a result of magnetic dissipation and reaches $\sigma \sim 1$ in a few outer-scale eddy turnover times. Then, $t_{\rm acc} \sim 10\,\ell/c$ as it would be in the case of fast reconnection ($\beta_R \sim 0.1$), driving particles up to the highest energies allowed by the system size (i.e., with particle Larmor radius $\rho_{\rm L} \sim \ell$).

Finally, we also expect that at the largest scales, magnetic reconfigurations can generate large-scale current sheets whose statistic is not well described as a self-similar sequence controlled by turbulent motions. In this case, the reconnection of the large-scale magnetic field might be responsible for particle acceleration up to the maximum available potential. Particle acceleration at these large-scale current sheets can extend up to the synchrotron burn-off limit of 100 MeV and beyond, thus powering the Crab Nebula gamma-ray flares (Lyutikov et al. 2017a, 2018). Therefore, in this model of the Crab Nebula radiation, magnetized turbulence with reconnecting current sheets can accelerate both the radio electrons and also produce the Crab gamma-ray flares.

6. The Turbulent Model of the Crab Nebula Radiation

6.1. Model Parameters

Above, in Sections 3 and 4, we described the one-dimensional spatial and temporal evolution of the flow and of the distribution function of the accelerated particles as functions of injection time and the magnetic field at present time in the Nebula. In this section, we calculate the resulting broadband spectrum: the synchrotron component and the inverse-Compton component of the nonthermal synchrotron emission, thermal dust emission, cosmic microwave background (CMB), and starlight photons.

Following Lyutikov et al. (2019), we assume that there are two acceleration mechanisms in the Crab Nebula: those from the termination shock (Component-I) and the reconnecting turbulence acceleration mechanism (Component-II). (The possibility of having two acceleration mechanisms in PWNs has been suggested previously by Kennel & Coroniti 1984b; Atoyan & Aharonian 1996; Bandiera et al. 2002; Meyer et al. 2010; Schweizer et al. 2013; Cerutti et al. 2014a; Olmi et al. 2014, 2015; Porth et al. 2014).

Component-I obeys the usual acceleration conditions of Fermi-I acceleration at the equatorial part of the pulsar wind; the properties of Component-II are discussed in Section 5. Both components are accelerated within the inner regions of the Nebula, though Component-II has more extended acceleration sites; see Figure 4 in Lyutikov et al. (2019). Here we ignore the difference in the sizes of the acceleration regions. With time, both components expand hydrodynamically and experience radiative cooling. Component-I is in the fast cooling regime, meaning that particles with minimal injected energy cool efficiently on the timescale of the PWN. Component-II is from magnetic reconnecting turbulence and is in the slow cooling regime, so that particles with minimal injected energy do not cool.

We assume that two populations of accelerated particles are injected into the inner region of the Nebula, Figure 3. Component-I's injected electron distribution has power-law index p_I, and minimum and maximum injection Lorentz factors $\gamma_{I_{min}}$ and $\gamma_{I_{max}}$. The values of p_I are restricted by the observed spectral power-law indices in the X-ray range, and the value of $\gamma_{I_{min}}$ is restricted by the observed peak and spectral power-law indices in the IR range. The maximum injection $\gamma_{I_{max}}$ is limited both by the observed break and the theoretical limit of synchrotron acceleration/burn-off, around 100 MeV (e.g., Lyutikov 2010).

For Component-II, the injected electron distribution has a broken power-law spectrum with indices p_{II1} and p_{II2}, minimum and maximum injection Lorentz factors $\gamma_{II_{min}}$ and $\gamma_{II_{max}}$, and break injection $\gamma_{II_{break}}$; p_{II1} is the power-law index below the injection break $\gamma_{II_{break}}$, and p_{II2} is the power-law index above $\gamma_{II_{break}}$. The minimum injection $\gamma_{II_{min}}$ is not restricted: it should be sufficiently low, ∼ a few hundreds at most, to have the radio spectrum extending down to below ∼100 MHz. The maximum injection $\gamma_{II_{max}}$ is similarly limited by the acceleration/burn-off. We illustrate these parameters in Figure 3. The spectrum below the break is determined by the observed radio spectrum. The break (approximately in the IR) is required for Component-II not to overshoot Component-I in the soft X-rays. (In the hard X-rays and gamma-rays, the two components contribute similarly.)

In our calculation, we fix $p_I = 2.2$ (this is derived from the X-ray spectrum of the Crab Nebula wisps), $p_{II1} = 1.6$ (which is derived from the radio spectral index $\alpha_r = 0.3$), and $\gamma_{II_{min}} = 200$
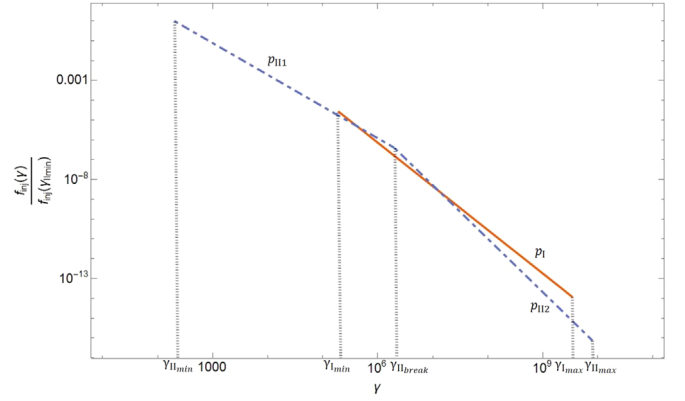

Figure 3. Illustration of parameters in Component-I and Component-II. Component-I is represented by the red solid curve, and Component-II is represented by the blue dashed curve. All parameter values are taken from Table 1, and we normalized the curve of Component-II to unity at its corresponding minimum injection Lorentz factor $\gamma_{II_{min}}$.

(corresponding to synchrotron frequency below a few tens of MHz). There are several fit parameters: magnetic field at present time B_{now}, $\gamma_{I_{min}}$, $\gamma_{II_{break}}$, $\gamma_{I_{max}}$, p_{II2}, $\gamma_{II_{max}}$, the relative normalization factor of Component-I and Component-II, and the overall normalization factors for each component. We explored these parameters and tried to fit the observational data of the IR index map, optical index map, and the broadband spectrum.

In the following sections, we first calculate the synchrotron spectrum in Section 6.2.1 and then the corresponding inverse Compton (IC) signal in Section 6.2.2. The overall spectrum and its evolution are calculated in Section 6.2.3, and the spatial evolution of spectral indices in the optical and radio in Section 7.

6.2. The Fitting Procedure

Fitting the broadband spectrum involving synchrotron and synchrotron self-Compton (SSC) components as well as other contribution for soft photons (e.g., dust, starlight, and CMB) involves numerous parameters and data measurements over a huge range of energies. This is a complicated task, which cannot be achieved in one go. Next we describe a novel procedure we developed to tackle this problem. It is somewhat akin to a bootstrap method, where numerous parameters are improved stepwise, trying to achieve the best fit.

Both components produce synchrotron emission, and, in addition, there are IC emission on the SSC photons, thermal dust emission, external starlight, and CMB. A wide range of particles and photon energies requires that Klein–Nishina (KN) effects be taken into account for the IC component. Next, we describe a novel procedure to self-consistently fit the synchrotron and IC processes (see Section 6.2.2) due to two-particle distributions.

6.2.1. The Synchrotron Component

We use the exact expression for local single particle spectral emissivity (Rybicki & Lightman 1979)

$$P(\omega, r, t) = \frac{\sqrt{3}}{2\pi} \frac{Be^3}{mc^2} F\left(\frac{\omega}{\omega_c}\right)$$

$$\omega_c = \frac{3}{2}\gamma^2 \frac{eB}{m_e c}$$

$$F(x) \equiv x \int_x^\infty K_{\frac{5}{3}}(\xi)\, d\xi \qquad (33)$$

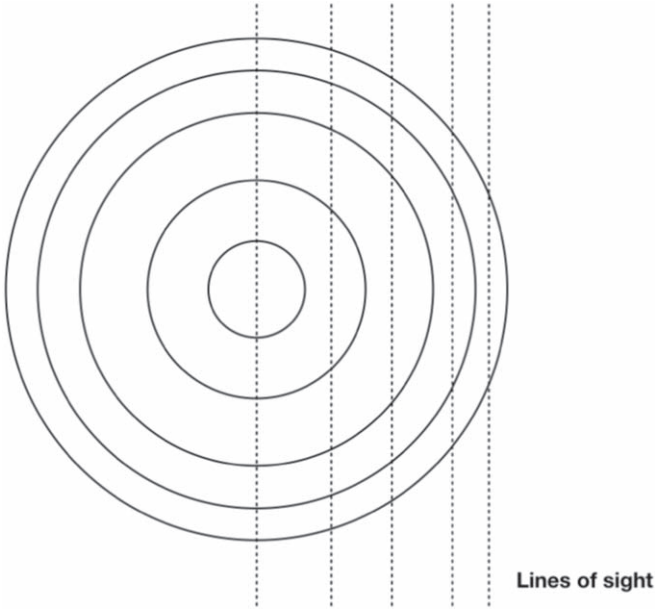where $K_{\frac{5}{3}}(\xi)$ is a Bessel function of the second kind.

Figure 4. Shell model of the Crab Nebula. We calculate the synchrotron emission along different lines of sight (dashed lines).

Given the temporal and the corresponding spatial evolution of the magnetic field, Equation (16) and the particles' Green's function, Equation (25), we calculate the spectral luminosity along a given line of sight at any moment t:

$$L(\omega, t) = \int_{r_{\min}}^{r_{\max}} dl \int N(\gamma, t, r) P(\omega, r, t)\, d\gamma, \qquad (34)$$

where the integration path passes through a different shell; see Figure 4.

In practice, we break the Nebula into a number of thin shells (180 in total in our calculation) and choose shell spacing equal in observed radii. The choice of equal spacing in the observed radii is important: equal spacing in presently observed radii corresponds to different durations of injection time for different shells; see Equation (13). We chose the innermost shell to be at $0.100\, R_{\rm PWN,now}$, and each shell has a width of $0.005\, R_{\rm PWN,now}$.

The ejection time for each shell is given by Equation (14), where $B_{\rm now}$ represents the current magnetic field in the Nebula and is a free parameter in our model. We then chose 10 lines of sight which are equally spaced in observed radii, i.e., 0.1 $R_{\rm PWN,now}$, 0.2 $R_{\rm PWN,now}$, ..., 1.0 $R_{\rm PWN,now}$. Using $N(t) = \int G(t, t_{\rm inj})\, dt_{\rm inj}$, for a given injection spectrum, we know the distribution function at each point in the Nebula at any given time. We can then calculate the spatially resolved synchrotron emissivity (see Section 6.2.1) and the IC power (see Section 6.2).

We adopt the following step-by-step method of fitting the observed spectrum from synchrotron emission:

1. We estimate $p_{\rm II2}$ from X-ray observations.
2. We fit the optical index map to estimate $B_{\rm now}$. Stronger $B_{\rm now}$ produces a sharper rise at outer shells, and a weaker $B_{\rm now}$ produces a milder rise at outer shells.
3. Once we have the estimate for $B_{\rm now}$, we are able to estimate $\gamma_{\rm I_{max}}$ and $\gamma_{\rm II_{max}}$ according to the broadband spectrum at the synchrotron limit region, where we expect both components to disappear above 100 MeV.

4. The requirement that Component-II does not overshoot Component-I in the X-ray region gives a range of allowed $\gamma_{\rm II_{break}}$.
5. We also fit the IR index map of the innermost shell, which is $\alpha \approx 0.3$ for lower frequencies and $\alpha \approx 0.5$ for higher frequencies. This gives $\gamma_{\rm II_{break}}$ and $\gamma_{\rm I_{min}}$.
6. Given the above estimates, we are then able to find the best value of the relative normalization factors of Component-I and Component-II.

6.2.2. The IC Component

Both the particle and photon distributions within the Nebula are very broad, so that for different parts of the distributions, IC scattering occurs both in the Thomson and Klein–Nishina regimes. The general expression for the differential cross section is (e.g., Aharonian 2004)

$$\frac{d\sigma_{KN}}{d\Omega} = \frac{3}{16\pi} \frac{\sigma_T}{(1 + x(1 - \cos\theta))}$$
$$\times \left(x(1 - \cos\theta) + \frac{1}{1 + x(1 - \cos\theta)} + \cos^2\theta \right), \tag{35}$$

where x is the initial photon energy in units of $m_e c^2$, and θ is the scattering angle in the frame where the electron is initially at rest.

Transformations of the directions and the energies of incoming, scattered photons and the lepton's velocity is a complicated exercise in Lorentz transformation (e.g., Aharonian & Atoyan 1981; Coppi & Blandford 1990; Atoyan & Aharonian 1996). In particular, Aharonian & Atoyan (1981) derived the angle-averaged scattering rate analytically, and Coppi & Blandford (1990) rederived the angle-averaged scattering rate by considering some standard asymptotic forms. In our work, we derived the angle-averaged outgoing photon energy, and then calculate it numerically.

The notations are the following. In the electron comoving frame K', x' is the energy of the incoming photon, x_1' is the energy of the outgoing photon, ψ' is the angle between the electron velocity and incoming photon direction, ψ_1' is the angle between the electron velocity and outgoing photon direction, δ' is the azimuthal angle, and θ' is the scattering angle. In the lab frame, we define x as the incoming photons' energy, x_1 as the outgoing photons' energy, and ψ as the angle between the electron velocity and incoming photon direction.

Combining Lorentz transformations

$$x' = \frac{x}{\gamma(1 + \beta\cos\psi')} \tag{36}$$

with Compton scattering

$$x_1' = \frac{x'}{1 + x'(1 - \cos\theta')}, \tag{37}$$

we find

$$x_1 = \frac{x\gamma(1 + \beta\cos\psi_1')}{\gamma(1 + \beta\cos\psi') + x(1 - \cos\theta')}. \tag{38}$$

The geometric relation between the scattering angle θ', azimuth angle δ', the angle between the incoming photon and electron ψ', and the angle between outgoing photons and

electron ψ_1' is

$$\cos \psi_1' = \cos \theta' \cos \psi' - \sin \theta' \cos \delta' \sin \psi', \qquad (39)$$

which gives

$$x_1 = \frac{x\gamma(1 + \beta(\cos \theta' \cos \psi' - \sin \theta' \cos \delta' \sin \psi'))}{\gamma(1 + \beta \cos \psi') + x(1 - \cos \theta')}. \qquad (40)$$

The Lorentz transformation for the angle is $\cos \psi' = \frac{\cos \psi - \beta}{1 - \beta \cos \psi}$, thus

$$x_1 = \frac{x\gamma\left(1 + \beta\left(\cos \theta' \frac{\cos \psi - \beta}{1 - \beta \cos \psi} - \sin \theta' \cos \delta' \sin \psi'\right)\right)}{\gamma\left(1 + \beta \frac{\cos \psi - \beta}{1 - \beta \cos \psi}\right) + x(1 - \cos \theta')}. \qquad (41)$$

Then, averaging over angles δ' and ψ, we have

$$x_1 = \frac{\csc^2 \frac{\theta'}{2}\left((\gamma - x \cos \theta') \ln\left(\frac{2\gamma - x \cos \theta' + x}{4\gamma^2\left(\frac{1}{2\gamma} - x \cos \theta' + x\right)}\right) + 2x\gamma^2(1 - \cos \theta')\right)}{4x\gamma}. \qquad (42)$$

Equation (42) is valid in the limit of $\gamma \gg 1$.

In order to fit the IC component, we adopt the step-by-step procedure of fitting the observed spectrum from IC emission:

1. For the sample of Lorentz factor of electrons (say $\gamma = 200$, $\gamma = 400$, ...), we calculated the corresponding number density of electrons n_e and made a table of values as n_e versus γ.
2. For the sample of incoming photon energies (say $x = 10^{-7}$ eV, $x = 2 \times 10^{-7}$ eV, ...), we calculated the corresponding number of incoming photons N_γ and made a table of values as N_γ versus x.
3. For the sample of outgoing photon energies x_1, we made a table of $N_{\text{scattered}}$ versus x_1, where $N_{\text{scattered}}$ is unknown and will be calculated in the following steps.
4. We pick values of γ, x, and x_1 from the tables and run the loop (e.g., $\gamma = 200$, $x = 10^{-7}$ eV, $x_1 = 10^5$ eV), and we solve Equation (42) to find the value of $\cos \theta'$.
5. Assuming that the solution of Equation (42) is $\cos \theta' = S(x, x_1, \gamma)$, then $d(\cos \theta') = S_{\max}(\check{x}, \check{x}_1, \check{\gamma}) - S_{\min}(\check{x}, \check{x}_1, \check{\gamma})$, for $\check{x} \in \left[x - \frac{dx}{2}, x + \frac{dx}{2}\right]$, $\check{x}_1 \in \left[x_1 - \frac{dx_1}{2}, x_1 + \frac{dx_1}{2}\right]$, and $\check{\gamma} \in \left[\gamma - \frac{d\gamma}{2}, \gamma + \frac{d\gamma}{2}\right]$, where dx, dx_1, and $d\gamma$ are the step lengths in the table.
6. Substituting the value of x', $\cos \theta'$ and $d \cos \theta'$ into Equation (35), we can calculate the corresponding differential cross section.
7. Then, if we substitute the corresponding number density of electrons n_e and the number particle of incoming photons N_γ (say, the ith row in the table is value n_{e_i} and the jth row in the table is value N_{γ_j}), the collision rate would be $n_{e_i} N_{\gamma_j} c\sigma$. We need to be aware that all variables above are in the rest frame of the electron.
8. Thus, the collision rate in the lab frame is $N_{\text{scattered}} = n_{e_i} N_{\gamma_j} c\sigma / \gamma_i$.
9. Finally, summing up over the table of values of electrons and multiply the scattered photon frequency, we will find $(\nu F(\nu))_{\text{scattered}} \propto \sum_{i,j} \nu x_1 N_{\text{scattered}} = \sum_{i,j} \nu x_1 n_{e_i} N_{\gamma_j} c\sigma / \gamma_i$.

We verified that the step-by-step procedure described here reproduces a number of analytical results (e.g., IC scattering of monoenergetic seed photons and monoenergetic electrons, IC scattering of monoenergetic seed photons, and power-law energy distribution of electrons).

6.2.3. The SSC Component

The model has a number of parameters; see Section 6.1. By adopting the step-by-step methods from Sections 6.2.1 and 6.2.2, we calculated the overall spectrum by adding the two synchrotron components and the SSC component.

The SSC emission is shown as curve 5 in Figure 6. Given that the model is very simple, e.g., 1D, and spans nearly 20 orders of magnitude in energy and some 7 orders of magnitude in flux, the fits were done "by eye." We found the best values of all parameters are $B_{\text{now}} = 2.7 \times 10^{-4}$ G, $\gamma_{\text{I}_{\max}} = 3.5 \times 10^9$, $\gamma_{\text{II}_{\max}} = 8.0 \times 10^9$, $p_{\text{II2}} = 2.7$, $\gamma_{\text{I}_{\min}} = 1.9 \times 10^5$, and $\gamma_{\text{II}_{\text{break}}} = 2.0 \times 10^6$. Component-II constitutes about 60% of the ejection energy and Component-I constitutes about 40% of the ejection energy. The numerical fitting program may be added in further work to improve the precision of parameter values, but for now, our results have good enough precision to demonstrate our model. We summarize all parameter values in Table 1.

We then substituted all of the parameter values from Table 1 into Equation (34) and calculated the broadband synchrotron spectrum in Figure 5, where we present the synchrotron emission from Component-I and Component-II as the yellow dotted line and purple dotted–dash line, respectively, and their combined contribution as the red solid line. As we can see, the low-energy synchrotron emission is dominated by Component-II, and the high-energy synchrotron emission is dominated by Component-I. In Section 6.2.2, we will use the broadband synchrotron spectrum as seed photons for the IC component calculation.

As shown in Figure 6, our purely SSC emission model with parameter values taken from Table 1 roughly reproduce the current broadband spectrum. The overall spectrum consists of three parts: Part I: 10^8–10^{14} Hz is the low-energy emission and is dominated by synchrotron emission from Component-II, which has a peak at around 10^{14} Hz. p_{II_2} does not affect the overall spectrum significantly; however, it will affect the IR spectral index map in Section 7. Part II: 10^{16}–10^{22} Hz is the mid-energy emission and is dominated by synchrotron emission from Component-I. Part III: 10^{22}–10^{28} Hz is the high-energy emission and has a peak around 10^{26} Hz. Part III is dominated by SSC emission when taking into account synchrotron emission from both Component-I and Component-II as seed photons.

6.2.4. Dust and Starlight Contributions

There is a big gap around the 10^{23}–10^{26} Hz region between the observational data and our numerical SSC emission. In

9

Table 1
Summary of Parameter Values

Parameters	B_{now} (G)	$\gamma_{I_{max}}$	$\gamma_{II_{max}}$	p_{II2}	$\gamma_{I_{min}}$	$\gamma_{II_{break}}$	E_{II}/E_{total}	E_I/E_{total}
Values	2.7×10^{-4}	3.5×10^9	8.0×10^9	2.7	1.9×10^5	2.0×10^6	0.6	0.4

Note. In this table, B_{now} is the magnetic field now. $\gamma_{I_{max}}$ is the maximum Lorentz factor of the injected electrons of Component-I. $\gamma_{II_{max}}$ is the maximum Lorentz factor of the injected electrons of Component-II. $\gamma_{II_{break}}$ is the middle break Lorentz factor of Component-II, where power-law indices are $p_{II1} = 1.6$ below $\gamma_{II_{break}}$ and p_{II2} above $\gamma_{II_{break}}$. $\gamma_{I_{min}}$ is the minimum Lorentz factor of injected electrons of Component-I. E_I is the energy of Component-I, E_{II} is the energy of Component-II, and E_{total} is the sum of the energies of Component-I and Component-II.
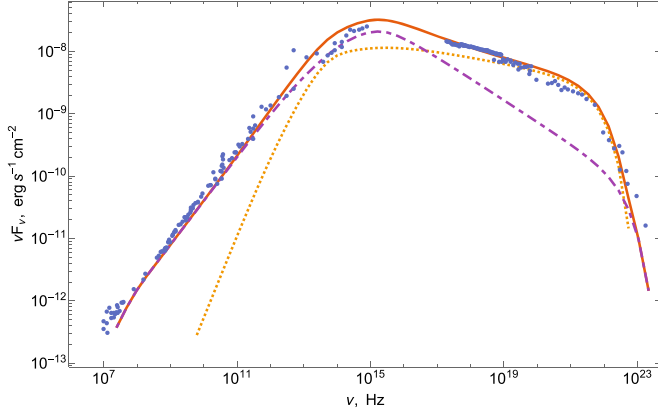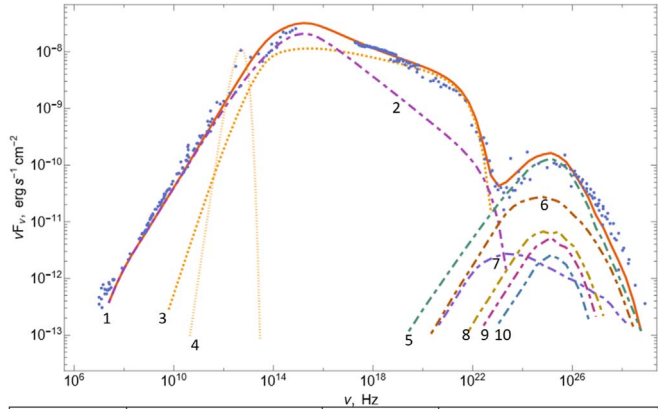

Figure 5. Comparison of observational data from Baldwin (1971), Baars et al. (1977), Macías-Pérez et al. (2010), Ney & Stein (1968), Grasdalen (1979), Green et al. (2004), Temim et al. (2006), and Kuiper et al. (2001), and the numerical result for the broadband spectrum. The dots represent observational data. The red solid line represents the total emission in the model. The purple and yellow dashed lines represent Component-I and Component-II.

Figure 7. Comparison of observed data from Veron-Cetty & Woltjer (1993) and the numerical result in the optical region. The wavelength range of the observational data is 0.5364–0.9241 μm. We set the Crab pulsar at 0.0. The green, blue, purple, and orange solid lines represent observational data from the west, east, south, and north directions, respectively. The red dashed line represents our numerical result at 0.7 μm.

Curve Number	Radiation Mechanism	Curve Number	Radiation Mechanism
1	Total spectrum	6	IC on dust
2	Component-II synchrotron	7	IC on CMB
3	Component-I Synchrotron	8	IC on starlight (peak at 0.1 eV)
4	Thermal dust emission	9	IC on starlight (peak at 0.3 eV)
5	SSC	10	IC on starlight (peak at 1.0 eV)

Figure 6. Broadband spectrum of Crab Nebula. The observational data are shown as blue dots (synchrotron data are the same as in Figure 5, and we add more data from Aharonian et al. 2006, Albert et al. 2008, and Abdo et al. 2010 above the synchrotron limit). Component-II (curve 2) and Component-I (curve 3) synchrotron emission are taken from Figure 5. SSC emission is shown as curve 5. IC on thermal dust emission (curve 4) is shown as curve 6. IC on CMB is shown as curve 7. IC on starlight is shown as curve 8 (peak energy at 0.1 eV), curve 9 (peak energy at 0.3 eV), and curve 10 (peak energy at 1.0 eV). The overall total spectrum is shown as curve 1 (here we ignore IC on starlight).
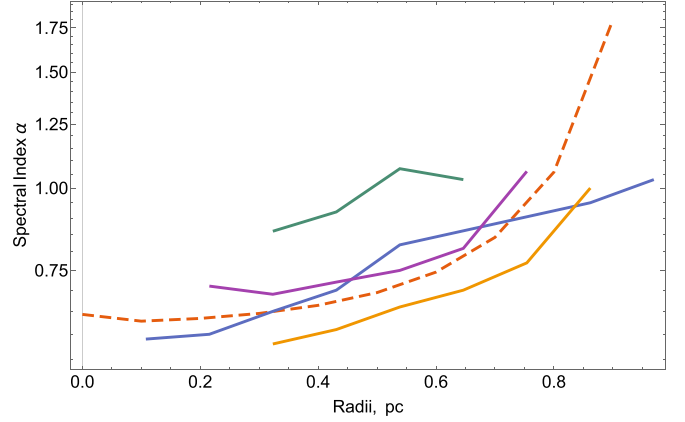
order to fill in this big gap, we consider additional IC photons on CMB and dust. First, we calculated the IC on seed photons, including CMB, Component-I, and Component-II. The IC on CMB is shown as curve 7 in Figure 6. As we can see, additional IC emission on CMB is not able to give an apparent rise or to fill in the gap around the 10^{23}–10^{26} Hz region. Thus, we need to add IC emission from dust.

We then consider thermal emission from dust with temperature 62 K, and the normalization factor is determined by fitting a small bump in the IR band around 5×10^{12} Hz. The thermal dust emission is shown as curve 4 in Figure 6. The associated IC emission gives a comparable contribution and fills in the gap. See curve 6 in Figure 6.

Our step-by-step method does not try to fit and calculate two synchrotron components and the IC emission at the same time. A fit-to-all (two synchrotron emission mechanism and IC emission) numerical algorithm with some statistical index checking could be implemented so that we can get better fitting results. But apparently, it costs more time to fit two physical processes at the same time. Jones (1968), Blumenthal & Gould (1970), Aharonian & Atoyan (1981), and Coppi & Blandford (1990) proposed different ways of calculating IC emission analytically and numerically; however, the way we adopted in this paper is the most acceptable way by trading off between time and precision.

Starlight photons also have IC emission within the nebula; thus, we investigate the effect of IC on starlight in this section.
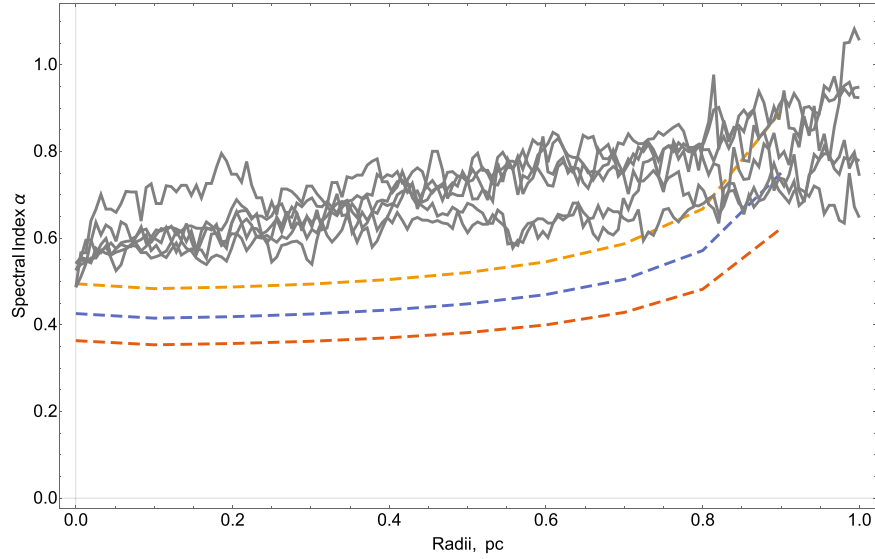
Figure 8. Comparison of the observed data and numerical result in the lower-frequency IR region. The wavelength range of the observational data is 3.6–8.0 μm. We set the Crab pulsar at 0.0. The solid lines represent observational data along different directions. The red dashed line represents our numerical result at 7.9 μm. The blue dashed line represents our numerical data at 5.3 μm. The orange dashed line represents our numerical data at 3.5 μm. Even though we are trying to match the innermost shell index instead of the whole index map, the trend seen in the whole index map is similar to our numerical model.
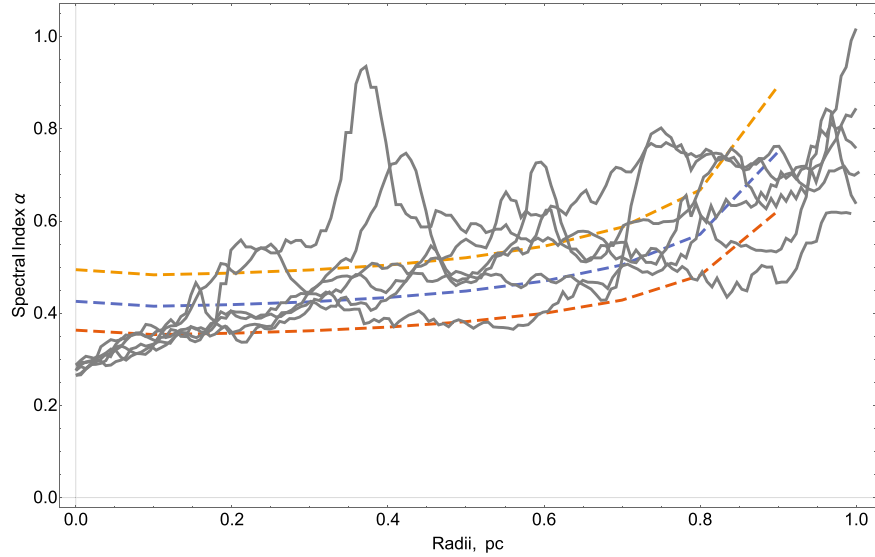

Figure 9. Comparison of observed data and numerical result in the higher-frequency IR region. The wavelength range in the observational data is 3.6–4.5 μm. We set the Crab pulsar at 0.0. The solid lines represent observational data along different directions. The red dashed line represents our numerical result at 7.9 μm. The blue dashed line represents our numerical data at 5.3 μm. The orange dashed line represents our numerical data at 3.5 μm. Even though we are trying to match the innermost shell index instead of the whole index map, the trend seen in the whole index map is similar to our numerical model.

We assume that seed photons of IC are from blackbody emission (for starlight with different temperatures corresponding to 0.1, 0.3, and 1.0 eV). Then, we adopted our step-by-step method from Section 6.2.2 again and calculated the corresponding IC emission.

In Figure 6, we present IC on starlight photons with peak energy at 0.1 eV (curve 8), 0.3 eV (curve 9), and 1.0 eV (curve 10), which are normalized to flux 1.0 eV cm^{-3} at the current time. Even for the highest IC emission on starlight in the case of peak energy at 0.1 eV, IC on starlight is way below the SSC. Thus, in later sections, we ignore the IC emission on starlight photons.

Finally, the total spectrum is shown as curve 1 in Figure 6 by combining Component-I and Component-II synchrotron, SSC, and IC on thermal dust emission and IC on CMB (here we ignore IC on starlight photons).

7. Spectral Maps in the Optical and IR

The spatial variations of the nonthermal spectrum have been identified as one of the drawbacks of the Kennel & Coroniti models (Reynolds 2009; Reynolds et al. 2017, and Section 1): the Kennel–Coroniti pure-MHD spherical advection model gives a constant spectral index with a sharp steepening at the

edge of the PWN. The addition of diffusion on top of the Kennel–Coroniti flow (Gratton 1972; Reynolds & Jones 1991; Tang & Chevalier 2012; Porth et al. 2016) has been proposed to explain the spectral steepening. Yet, the diffusion model cannot predict the change of the source size with photon energy.

Our method has the ability to reproduce the observed spectral index map, which is gradually steepening from the innermost shell to the edge of the PWN. In order to calculate the spectral index map, we consider our shell model in Figure 4. Each shell has the same parameters but only the injection time is different. The injection time needs be calculated using Equation (14). For any given injection time, we are able to calculate the emissivity within each shell. By summing up the emission from each shell, we are able to calculate the total emission along each line of sight.

In our work, we calculate the emission along each line of sight in the IR (7.9, 5.3, and 3.5 μm) and optical wavelengths (0.7 μm), and then we use them to plot the spectral index map at each frequency. Results are presented in Figures 7–9.

Figures 7–9 show that the spectral index maps from radio to IR are consistent with observational results, thus demonstrating that our model can generally reproduce the evolution of the spectral indices in IR and optical.

8. Conclusion

In this paper, following Lyutikov et al. (2019), we further develop a turbulent model of the Crab Nebula, and by extension, of PWNs in general. We demonstrate that turbulence that developed in the magnetized post-shock wind can consistently resolve a number of problems of the Kennel and Coroniti model, both theoretical and observational. Turbulence and the ensuing reconnection destroy the magnetic flux, resolving the long-standing sigma paradox and explain the origin and spectrum of radio electrons, gamma-ray flares, and the spectral evolution of the flow. With a simple 1D model, we are able to fit, within a factor of a few, the broadband spectrum that stretches over 20 orders of magnitude in frequency. Importantly, the model suggests that reconnection is an important particle acceleration mechanism in a major astro-physical object—and, by extension, may be important/dominant in other astrophysical high-energy sources.

We advocate two acceleration mechanisms that produce two separate particle components: Component-I originates from particles accelerated at the termination shock, presumably via the Fermi-I acceleration mechanism. Component-I dominates from optical to X-ray wavelengths and produces mostly the bright X-ray torus. Component-II is generated by magnetized turbulence that produces reconnecting current sheets of different sizes in the bulk of the Nebula. Particles are then accelerated by magnetic reconnection in the current layers and by scattering off turbulent fluctuations. Both the hard radio spectrum of Component-II and the requirement that rare reconnection events produce gamma-ray flares, require regions with high magnetization, $\sigma \gg 1$.

Thus, we argue that the radio-emitting leptons are acceler-ated by the same mechanism as GeV-emitting leptons, but are different from the X-ray-emitting ones. This is different from Olmi et al. (2014, 2015), where the two populations were nonoverlapping in energy. One of the major advantages of our model is that it is physically motivated and not just an ad hoc parameterization.

The model also explains low injection Lorentz factor for Component-II, $\gamma_{\text{II,min}}$ (see the more detailed discussion in Lyutikov et al. 2019). At midlatitudes, the pulsar wind is relatively slow, $\gamma_w \sim 10^2$, and highly magnetized, $\sigma_w \sim 10^3$. Thus, the total energy per particle (in terms of $m_e c^2$) is $\gamma_p \sim \gamma_w \sigma_w \sim 10^5$. Within the striped part of the wind, this total energy is given to the particles, producing the break at $\gamma_{I,\text{min}}$. At the intermediate attitudes, where the wind is not striped, only the bulk energy is thermalized, giving $\gamma_{\text{II,min}} \sim \gamma_w \sim 10^2$.

There are a number of issues that remain to be resolved. First, our 1D model naturally cannot reproduce azimuthal variations in the properties of the Crab Nebula. Presumably they originate from the intrinsic anisotropy of the wind and mildly relativistic velocities (and corresponding Doppler corrections) of the shocked flow in the innermost parts of the Nebula.

A more accurate evaluation of the particle energization near the cut-off energy would require a kinetic equation that also includes the effect of particle diffusion. In future work, we want to develop a more refined kinetic model that includes particle diffusion. Synchrotron radiation losses could also be added in Equation (32). However, the synchrotron cooling of the radio electrons is negligible in the Crab Nebula. Particle acceleration by reconnection electric fields also do not suffer significant synchrotron losses as the particle pitch angle is aligned with the magnetic field. On the other hand, the synchrotron losses in Fermi-II acceleration would become significant at much higher particle energies. We intend to explore their role with particle-in-cell simulations in subse-quent works.

The main theoretical unsolved problem that the current model depends on is the suggestion that magnetic reconnection can indeed produce a spectrum with $p = 1.6$, Section 5. Another issue is the sheer number of radio-emitting electrons (Atoyan 1999).

ORCID iDs

Maxim Lyutikov ⬤ https://orcid.org/0000-0001-6436-8304
Tea Temim ⬤ https://orcid.org/0000-0001-7380-3144
Luca Comisso ⬤ https://orcid.org/0000-0001-8822-8031

References

Abdo, A. A., Ackermann, M., Ajello, M., et al. 2010, ApJ, 708, 1254
Abdo, A. A., Ackermann, M., Ajello, M., et al. 2011, Sci, 331, 739
Aharonian, F., Akhperjanian, A. G., Bazer-Bachi, A. R., et al. 2006, A&A, 457, 899
Aharonian, F. A. 2004, Very High Energy Cosmic Gamma Radiation: A Crucial Window on the Extreme Universe (Singapore: World Scientific)
Aharonian, F. A., & Atoyan, A. M. 1981, Ap&SS, 79, 321
Albert, J., Aliu, E., Anderhub, H., et al. 2008, ApJ, 674, 1037
Arons, J. 2007, arXiv:0708.1050
Arons, J. 2012, SSRv, 173, 341
Atoyan, A. M. 1999, A&A, 346, L49
Atoyan, A. M., & Aharonian, F. A. 1996, MNRAS, 278, 525
Baars, J. W. M., Genzel, R., Pauliny-Toth, I. I. K., & Witzel, A. 1977, A&A, 500, 135

Baldwin, J. E. 1971, in IAU Symp. 46, The Crab Nebula, ed. R. D. Davies & F. Graham-Smith (Dordrecht: Reidel), 22

Bandiera, R., Neri, R., & Cesaroni, R. 2002, A&A, 386, 1044

Bessho, N., & Bhattacharjee, A. 2012, ApJ, 750, 129

Bietenholz, M. F., Kassim, N., Frail, D. A., et al. 1997, ApJ, 490, 291

Bietenholz, M. F., & Kronberg, P. P. 1991, ApJ, 368, 231

Blandford, R., & Eichler, D. 1987, PhR, 154, 1

Blumenthal, G. R., & Gould, R. J. 1970, RvMP, 42, 237

Buehler, R., Scargle, J. D., Blandford, R. D., et al. 2012, ApJ, 749, 26

Carbone, V., Veltri, P., & Mangeney, A. 1990, PhFlA, 2, 1487

Cerutti, B., Werner, G. R., Uzdensky, D. A., & Begelman, M. C. 2012, ApJL, 754, L33

Cerutti, B., Werner, G. R., Uzdensky, D. A., & Begelman, M. C. 2014a, PhPl, 21, 056501

Cerutti, B., Werner, G. R., Uzdensky, D. A., & Begelman, M. C. 2014b, ApJ, 782, 104

Chauvin, M., Florén, H.-G., Friis, M., et al. 2017, NatSR, 7, 7816

Chauvin, M., Florén, H.-G., Friis, M., et al. 2018, MNRAS, 477, L45

Chauvin, M., Florén, H.-G., Jackson, M., et al. 2016, MNRAS, 456, L84

Chevalier, R. A. 2005, ApJ, 619, 839

Clausen-Brown, E., & Lyutikov, M. 2012, MNRAS, 426, 1374

Comisso, L., & Bhattacharjee, A. 2016, JPlPh, 82, 595820601

Comisso, L., Huang, Y. M., Lingam, M., Hirvijoki, E., & Bhattacharjee, A. 2018, ApJ, 854, 103

Comisso, L., Lingam, M., Huang, Y.-M., & Bhattacharjee, A. 2016, PhPl, 23, 100702

Comisso, L., Lingam, M., Huang, Y. M., & Bhattacharjee, A. 2017, ApJ, 850, 142

Comisso, L., & Sironi, L. 2018, PhRvL, 121, 255101

Comisso, L., & Sironi, L. 2019, ApJ, 886, 122

Coppi, P. S., & Blandford, R. D. 1990, MNRAS, 245, 453

Coroniti, F. V. 1990, ApJ, 349, 538

de Jager, O. C., Harding, A. K., Michelson, P. F., et al. 1996, ApJ, 457, 253

Dean, A. J., Clark, D. J., Stephen, J. B., et al. 2008, Sci, 321, 1183

del Zanna, L., Amato, E., & Bucciantini, N. 2004, A&A, 421, 1063

Fawley, W. M., Arons, J., & Scharlemann, E. T. 1977, ApJ, 217, 227

Grasdalen, G. L. 1979, PASP, 91, 436

Gratton, L. 1972, Ap&SS, 16, 81

Green, D. A., Tuffs, R. J., & Popescu, C. C. 2004, MNRAS, 355, 1315

Guo, F., Li, H., Daughton, W., & Liu, Y.-H. 2014, PhRvL, 113, 155005

Harding, A. K., & Muslimov, A. G. 1998, ApJ, 508, 328

Hibschman, J. A., & Arons, J. 2001, ApJ, 560, 871

Hoshino, M., & Lyubarsky, Y. 2012, SSRv, 173, 521

Jones, F. C. 1968, PhRv, 167, 1159

Kagan, D., Sironi, L., Cerutti, B., & Giannios, D. 2015, SSRv, 191, 545

Kennel, C. F., & Coroniti, F. V. 1984a, ApJ, 283, 694

Kennel, C. F., & Coroniti, F. V. 1984b, ApJ, 283, 710

Komissarov, S. S. 2012, arXiv:1207.3192

Komissarov, S. S., & Lyubarsky, Y. E. 2004, MNRAS, 349, 779

Kuiper, L., Hermsen, W., Cusumano, G., et al. 2001, A&A, 378, 918

Lazarian, A., & Vishniac, E. T. 1999, ApJ, 517, 700

Lemoine, M. 2019, PhRvD, 99, 083006

Liu, Y.-H., Guo, F., Daughton, W., Li, H., & Hesse, M. 2015, PhRvL, 114, 095002

Loureiro, N. F., & Boldyrev, S. 2017, PhRvL, 118, 245101

Lyubarsky, Y., & Kirk, J. G. 2001, ApJ, 547, 437

Lyubarsky, Y., & Liverts, M. 2008, ApJ, 682, 1436

Lyubarsky, Y. 2005, MNRAS, 358, 113

Lyutikov, M. 2006, NJPh, 8, 119

Lyutikov, M. 2010, MNRAS, 405, 1809

Lyutikov, M., & Blandford, R. 2003, arXiv:astro-ph/0312347

Lyutikov, M., Komissarov, S., Sironi, L., & Porth, O. 2018, JPlPh, 84, 635840201

Lyutikov, M., Sironi, L., Komissarov, S. S., & Porth, O. 2017a, JPlPh, 83, 635830601

Lyutikov, M., Sironi, L., Komissarov, S. S., & Porth, O. 2017b, JPlPh, 83, 635830602

Lyutikov, M., Temim, T., Komissarov, S., et al. 2019, MNRAS, 489, 2403

Lyutikov, M., & Uzdensky, D. 2003, ApJ, 589, 893

Macías-Pérez, J. F., Mayet, F., Aumont, J., & Désert, F. X. 2010, ApJ, 711, 417

Mallet, A., Schekochihin, A. A., & Chandran, B. D. G. 2017, MNRAS, 468, 4862

Matthaeus, W. H., & Lamkin, S. L. 1986, PhFl, 29, 2513

Meyer, M., Horns, D., & Zechlin, H. S. 2010, A&A, 523, A2

Ney, E. P., & Stein, W. A. 1968, ApJL, 152, L21

Olmi, B., del Zanna, L., Amato, E., Bandiera, R., & Bucciantini, N. 2014, MNRAS, 438, 1518

Olmi, B., del Zanna, L., Amato, E., & Bucciantini, N. 2015, MNRAS, 449, 3149

Planck Collaboration, Aghanim, N., Akrami, Y., et al. 2018, arXiv:1807.06207

Porth, O., Buehler, R., Olmi, B., et al. 2017, SSRv, 207, 137

Porth, O., Komissarov, S. S., & Keppens, R. 2013, MNRAS, 431, L48

Porth, O., Komissarov, S. S., & Keppens, R. 2014, MNRAS, 438, 278

Porth, O., Vorster, M. J., Lyutikov, M., & Engelbrecht, N. E. 2016, MNRAS, 460, 4135

Rees, M. J., & Gunn, J. E. 1974, MNRAS, 167, 1

Reynolds, S. P. 2009, ApJ, 703, 662

Reynolds, S. P., & Jones, F. C. 1991, ICRC (Dublin), 2, 400

Reynolds, S. P., Pavlov, G. G., Kargaltsev, O., et al. 2017, SSRv, 207, 175

Ritacco, A., Macías-Pérez, J. F., Ponthieu, N., et al. 2018, A&A, 616, A35

Rybicki, G. B., & Lightman, A. D. 1979, Radiative Processes in Astrophysics (New York: Wiley)

Schweizer, T., Bucciantini, N., Idec, W., et al. 2013, MNRAS, 433, 3325

Sironi, L., Giannios, D., & Petropoulou, M. 2016, MNRAS, 462, 48

Sironi, L., & Spitkovsky, A. 2014, ApJL, 783, L21

Tanaka, S. J., Toma, K., & Tominaga, N. 2018, MNRAS, 478, 4622

Tang, X., & Chevalier, R. A. 2012, ApJ, 752, 83

Tavani, M., Bulgarelli, A., Vittorini, V., et al. 2011, Sci, 331, 736

Temim, T., Gehrz, R. D., Woodward, C. E., et al. 2006, AJ, 132, 1610

Uzdensky, D. A., & Loureiro, N. F. 2016, PhRvL, 116, 105003

Veron-Cetty, M. P., & Woltjer, L. 1993, A&A, 270, 370

Werner, G. R., & Uzdensky, D. A. 2017, ApJL, 843, L27

Werner, G. R., Uzdensky, D. A., Cerutti, B., Nalewajko, K., & Begelman, M. C. 2016, ApJL, 816, L8

Zenitani, S., Hesse, M., & Klimas, A. 2009, ApJ, 696, 1385

Zenitani, S., & Hoshino, M. 2001, ApJL, 562, L63

Zhdankin, V., Werner, G. R., Uzdensky, D. A., & Begelman, M. C. 2017, PhRvL, 118, 055103

Zrake, J., & Arons, J. 2017, ApJ, 847, 57